Icarus 387 (2022) 115184

Contents lists available at ScienceDirect

Icarus

journal homepage: www.elsevier.com/locate/icarus

Research Paper

Modeling the production of submicroscopic iron in the lunar highlands

A.P. Jordan [a,b,*], M.L. Shusterman [c], C.J. Tai Udovicic [d]

[a] Institute for the Study of Earth, Oceans, and Space, University of New Hampshire, Durham, NH, USA
[b] Solar System Exploration Research Virtual Institute, NASA Ames Research Center, Moffett Field, CA, USA
[c] School of Earth and Space Exploration, Arizona State University, Tempe, AZ, USA
[d] Northern Arizona University, Flagstaff, AZ, USA

ARTICLE INFO

Keywords:
Moon
Surface
Regoliths
Impact processes
Solar wind
Cosmic rays

ABSTRACT

Micrometeoroid impacts, solar wind bombardment, and dielectric breakdown driven by solar energetic particles all potentially alter the optical properties of the lunar regolith by creating submicroscopic metallic iron ($smFe^0$), which includes both nanophase (<33 nm) and microphase (>33 nm) iron. We create a simple model that describes the time-dependent accumulation of optically active $smFe^0$ in the lunar highlands. Our model synthesizes recent analyses of how space weathering processes form $smFe^0$-bearing agglutinates and rims on soil grains and how impact gardening controls the exposure time of these grains. It successfully reproduces the results of a prior analysis of the formation of $smFe^0$ in the highlands, particularly in regard to nanophase iron, showing that there is consistency among diverse analyses of Apollo samples and of orbital observations. We find that the results of our model are not consistent with the solar wind directly forming $smFe^0$ (although the solar wind may play a role in optical maturation via hydrogen implantation). Our model results are consistent with $smFe^0$ in the lunar highlands being created mainly by micrometeoroid impacts, with a possible contribution from dielectric breakdown weathering.

1. Introduction

The Moon is exposed to processes, such as bombardment by charged particles and micrometeoroids, that alter the optical properties of the regolith (for recent reviews, see Domingue et al., 2014 and Pieters and Noble, 2016). These processes can amorphize mineral surfaces and produce submicroscopic metallic iron ($smFe^0$) found either in amorphous rims on grains or in agglutinates (glass-welded aggregates) (e.g., Keller and McKay, 1997; Keller and Clemett, 2001). The larger, microphase inclusions (~40 nm to 2 μm) darken the reflectance spectrum in the visible and near-infrared, while smaller, nanophase inclusions ($\lesssim$40 nm) both darken and redden the reflectance spectrum (Britt and Pieters, 1994; Noble et al., 2007; Lucey and Riner, 2011).

A critical outstanding question is the relative role each weathering element plays in the maturation of regolith that can be observed optically. The solar wind creates inclusion-poor, amorphous rims on soil grains (Keller and McKay, 1997). Micrometeoroid impacts and solar wind sputtering may create inclusion-rich, vapor-deposited rims and agglutinates (e.g., Keller and McKay, 1997; Keller and Clemett, 2001). In addition, there may be another process at work: dielectric breakdown ("sparking") caused by extreme charging during large solar energetic particle (SEP) events (Jordan et al., 2014). Breakdown may produce inclusion-rich deposits at rates slightly less than impacts (Jordan et al., 2019; Jordan, 2021). All three processes vary with latitude, and the solar wind and dielectric breakdown should also be affected by magnetic fields, whether in Earth's magnetotail or in the Moon's magnetic anomalies (e.g., Hemingway et al., 2015; Sim et al., 2017; McFadden et al., 2019; Trang and Lucey, 2019; Jordan, 2021; Jordan et al., 2022). In addition, some have concluded that the solar wind may dominate the production of smaller iron inclusions, while micrometeoroids dominate the production of larger sizes (Kramer et al., 2011; Trang and Lucey, 2019; Blewett et al., 2021).

Consequently, determining the rate at which optically active $smFe^0$ is created can help us constrain the relative roles of the three potential weathering processes. Four studies can help. The first derived a function describing the growth of the abundance of agglutinitic grains in lunar soil (Mendell and McKay, 1975). The second measured the rate at which space weathered rims grow on soil grains and found that the two types of rims (solar wind–created and vapor-deposited) grow on timescales of ~1–10 Myr of exposure to the solar wind (Keller et al., 2021). The third study developed a simple method to estimate how long impact-gardened regolith has been exposed to a given space weathering process as a function of the working depth of that process (Jordan et al., 2013). Impact gardening buries weathered regolith grains and exposes shielded grains from the subsurface, preventing

* Correspondence to: Morse Hall Rm. 106A, 8 College Rd., Durham, NH 03824, USA.
E-mail address: a.p.jordan@unh.edu (A.P. Jordan).

https://doi.org/10.1016/j.icarus.2022.115184
Received 29 March 2022; Received in revised form 5 July 2022; Accepted 9 July 2022
Available online 14 July 2022

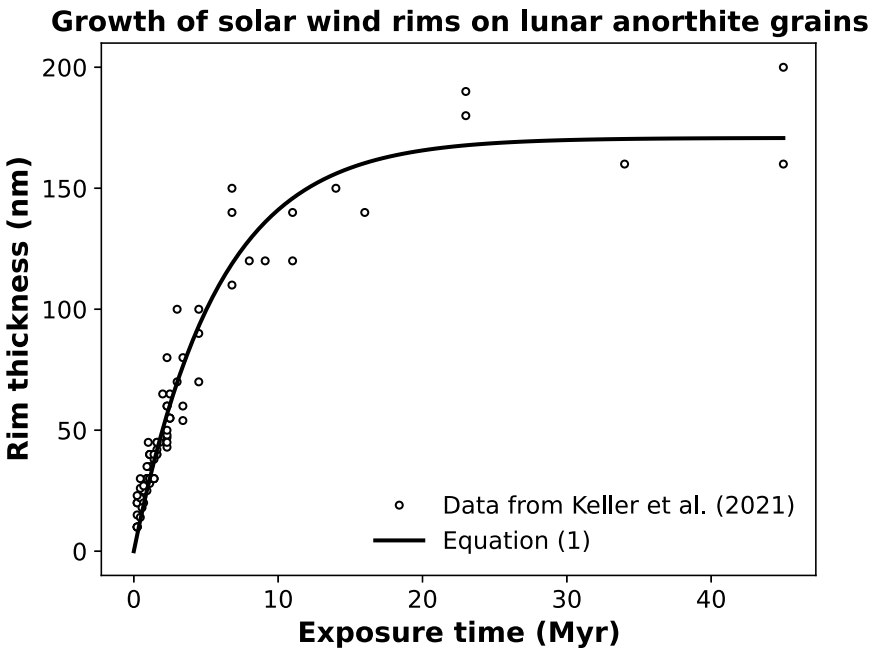

Fig. 1. The thickness of a solar wind rim on a soil grain (circles) grows as a function of the time the grain has been exposed to the solar wind (data from Keller et al., 2021). The maximum thickness (T_{max}) is reached after ~20 Myr. Our model for rim growth (Eq. (1)) best fits the data for T_{max} = 171 nm and τ_{SpWe} = 5.7 Myr (black curve). The 1σ uncertainties of these values are 4.8 nm and 0.3 Myr, and $R^2 = 0.94$.

them from being continuously exposed to space weathering process. In other words, because the solar wind, SEPs, and micrometeoroid impacts have different working depths in the regolith, grains are exposed to each process for a different length of time. The final study determined the rates at which two size fractions of submicroscopic iron—>33 nm microphase iron, or mpFe^0, and <33 nm nanophase iron, or npFe^0—accumulate in the highlands of the Moon (Tai Udovicic et al., 2021). (These sizes are different from those mentioned above because the maps of npFe^0 and mpFe^0 used by Tai Udovicic et al., 2021 were created using the smFe^0 size ranges defined by Morris, 1980; see Trang and Lucey, 2019.)

In this paper, we synthesize the results from these four studies to develop a straightforward model that describes the time-dependent accumulation of npFe^0 and mpFe^0 in the lunar highlands. Our model successfully reproduces the results of Tai Udovicic et al. (2021), placing critical constraints on the processes that optically mature the lunar regolith.

2. A model for the formation of submicroscopic iron in the highlands

2.1. The growth of submicroscopic iron in highland soil

Submicroscopic iron is found in all size fractions of the regolith, but the spectral reflectance of the Moon is dominated by the finest fraction (~15 μm) (Pieters et al., 1993; Lucey, 2006). The agglutinitic component of the soil contains most of the mpFe^0 (e.g., James et al., 2002; Basu, 2005; Pieters and Noble, 2016). On the other hand, the majority of optically active npFe^0 is found in space-weathered rims: as the average grain diameter approaches the finest fraction, the associated abundance of agglutinates increases only slightly, whereas the abundance of surface-correlated npFe^0 increases significantly (Taylor et al., 2001, 2010).

We consider first the growth of npFe^0. We assume that the npFe^0 is randomly distributed throughout these rims, which is reasonable because we model the abundance of npFe^0 on size-scales ($\gtrsim$10 km^2) much larger than the size-scale of individual grains. In other words, although the density of npFe^0 in a single grain's rim may depend on the composition of that grain or its vapor deposits (e.g., Keller and McKay, 1997), we use orbital observations that average together a very large number of grains of various compositions. Thus, we can assume that there is an average density of npFe^0 in grain rims. Given this, it is reasonable to assume that the abundance of npFe^0 is linearly proportional to the volume of the rims. Because rims are thin with respect to their host grains, the volume of a given rim is approximately the product of the grain's surface area and the rim's thickness. We consider the growth of both solar wind and deposited rims.

The growth of solar wind rims on grains of anorthite – whether from the mare or highlands – is well-constrained. Keller et al. (2021) showed that the rim thickness on a grain depends on the time the grain has been exposed to the solar wind. The thickness can be fit by a simple function:

$$T(t_{SpWe}) = T_{max}\left[1 - \exp\left(\frac{-t_{SpWe}}{\tau_{SpWe}}\right)\right] \quad (1)$$

where T is the thickness (in nm), T_{max} is the maximum thickness (~170 nm), t_{SpWe} is how long the grain has been exposed to space weathering, and τ_{SpWe} is the characteristic timescale (~6 Myr) for rim growth (Fig. 1). The reason for the maximum thickness is likely because there is a maximum penetration depth of the solar wind ions that create amorphous rims (Keller et al., 2021).

Although amorphous solar wind rims can contain some npFe^0 (Keller and McKay, 1997; Keller et al., 2000), the majority of these inclusions is found in depositional rims formed by some combination of solar wind sputtering and micrometeoroid bombardment (Hapke et al., 1975; Keller and McKay, 1997; Hapke, 2001). The thickness of depositional rims exhibits significant scatter as a function of exposure time; this may be due to the stochastic nature of micrometeoroid bombardment, both in energy and frequency (Keller et al., 2021). Despite this, the average thickness of deposited rims in a soil (rather than on an individual grain) should also follow Eq. (1), but with values of T_{max} and τ_{SpWe} that differ from those of solar wind rims.

This can be seen by considering the fact that the average thickness depends on the rates at which the rims are being created and the grains being destroyed by impacts (e.g., McKay et al., 1974). Initially, the average thickness grows linearly with exposure time t_{SpWe} because fresh

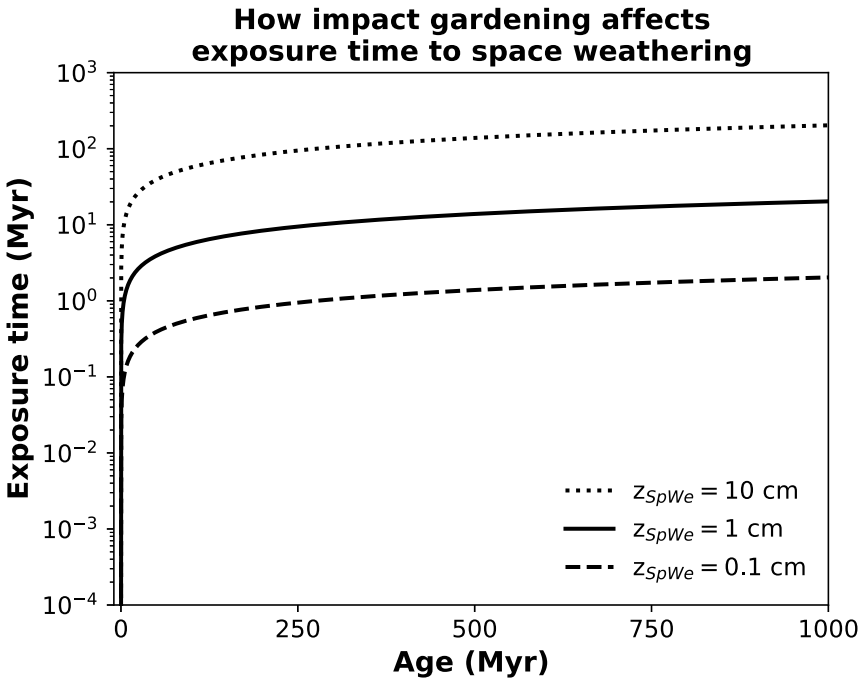

Fig. 2. How the exposure time of impact gardened soil to a given space weathering process depends on the soil's age and on the functional depth of that process (z_{SpWe}) for three values of z_{SpWe} (see Eq. (5)). Older soils have been more gardened, exposing more grains to the weathering process, so the exposure time increases with age. In addition, grains are exposed for more time to processes that are more penetrating (i.e., have a greater z_{SpWe}).

regolith has so few rim-bearing grains that their destruction is unlikely. Eventually, the number of grains with rims is sufficiently high that rim-bearing grains are destroyed at the rate at which rims are created. At about this time, the average rim thickness in the soil has reached a steady state. Consequently, it seems reasonable to assume that the average thickness of depositional rims follows Eq. (1). As mentioned above, the abundance of optically active npFe^0 is proportional to rim thickness and thus has the same functional form as Eq. (1).

For the growth of mpFe^0, we assume that, to first order, its abundance is proportional to the total volume of agglutinitic material in the soil. The abundance of agglutinates likely has the same functional form as does Eq. (1) (Mendell and McKay, 1975), so the abundance of mpFe^0 does, as well. We do note that the formation of mpFe^0 may be more complex than we assume, as some may be formed by the coalescing of npFe^0 when npFe^0-bearing rims and agglutinates are melted by impacts (e.g., see the discussions in Basu, 2005 and Pieters and Noble, 2016). As a result, the abundance of mpFe^0 might continue growing after the volume of agglutinitic material has reached a steady state, e.g., mpFe^0-poor agglutinates may become mpFe^0-rich via repeated melting. We find, however, no evidence that the growth of mpFe^0 deviates from our assumed functional form in this way (see Sections 3 and 4).

We conclude, then, that both size-ranges of highland smFe^0 follow this equation:

$$s(t) = s_{max} - s_{\Delta} \exp\left(\frac{-t_{SpWe}(t)}{\tau_{SpWe}}\right) \tag{2}$$

where s is the weight percent (wt%) of smFe^0, and s_{max} is the steady-state wt% of smFe^0, s_{Δ} is the difference between the steady-state abundance and the initial abundance, t is the age of the soil, t_{SpWe} is a function of t, and τ_{SpWe} is the characteristic timescale of growth for the size-range under consideration. The values of s_{max} and τ_{SpWe} and the function $t_{SpWe}(t)$ all depend on the space weathering process being described.

2.2. The exposure time of the lunar regolith

To model the weight percent of smFe^0 as a function of time, we must estimate $t_{SpWe}(t)$, a function that describes how the exposure time of the soil to a given space weathering process increases with time. The exposure time depends on how long soil grains have spent at depths shallow enough for them to be space weathered. Thus, $t_{SpWe}(t)$ is controlled by how impacts mix, or garden, the regolith (e.g., Jordan et al., 2013).

The top layer of regolith has been thoroughly gardened (down to tens of centimeters on timescales of up to ~1 Gyr), as shown by the fact that various soil maturity indices are constant throughout the layer (Morris, 1978). We make the simplifying assumption that all grains in the gardened layer (i.e., the in-situ reworking zone) have spent about equal time at all depths from the surface to the bottom of the gardened layer (we discuss this assumption below). Consequently, all the soil grains have been exposed to a given space weathering process for as long as they have been at depths shallow enough for that process to operate on them (e.g., O'Brien and Byrne, 2021). This means that the ratio of the soil's exposure time to its age is approximately the ratio of the characteristic penetration depth of space weathering (z_{SpWe}) to the depth of gardening (z_g):

$$\frac{t_{SpWe}(t)}{t} = \frac{z_{SpWe}}{z_g(t)} \tag{3}$$

In other words, the soil's grains within the gardened zone have spent all their lifetimes (t) within that zone (i.e, at depths $\leq z_g$), but only some of that time (t_{SpWe}) at depths to which a given space weathering process can operate ($\leq z_{SpWe}$). As a result, the typical exposure time of all gardened grains in a soil to a shallow process, like solar wind bombardment, is much less than their exposure time to a deeper process, like micrometeoroid impacts.

Both t_{SpWe} and z_g are functions of t. This equation applies only for $z_g > z_{SpWe}$, because when $z_g < z_{SpWe}$, $t_{SpWe}(t) = t$, i.e., all gardened grains have been exposed to a given space weathering process for the lifetime of the soil. In this study, we consider only cases where $z_g > z_{SpWe}$. This is similar to Jordan et al. (2013), except that they used the gardening function of Arnold (1975). Here, we use the function from Morris (1978) that provides a better fit to the Apollo samples (e.g., see Fig. 3 of Morris, 1978).

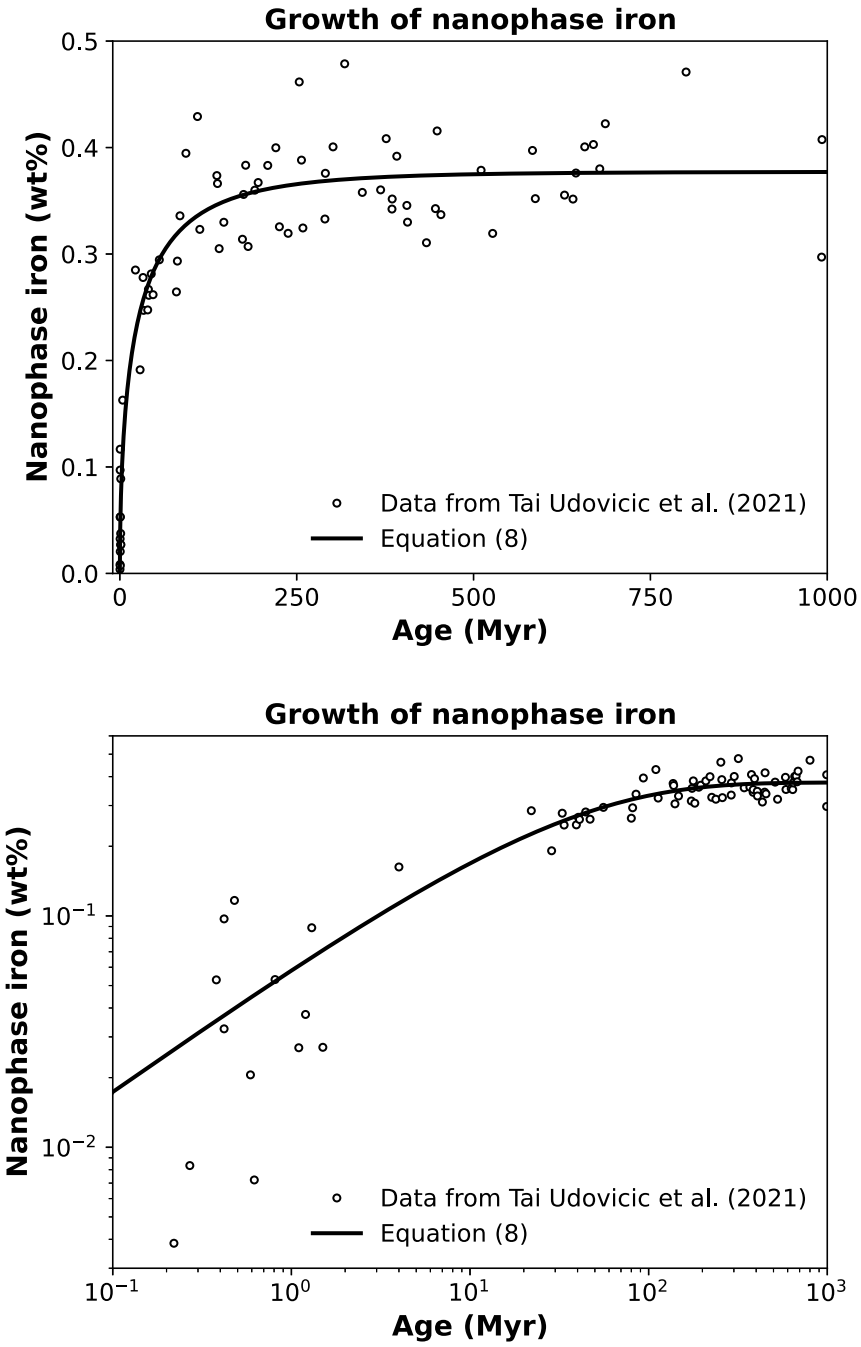

Fig. 3. Our model provides a good fit to how the abundance of nanophase iron in the highlands depends on the age of the soil. Both plots show the same data and model output; the top has a linear scale and the bottom a logarithmic scale. The data are from the study of Tai Udovicic et al. (2021) (for uncertainties, please see their Fig. 3). The best fit using Eq. (8) has $n_{max} = 0.38$ wt% and $\sum_i (z_i/\tau_i) = 0.37$ cm Myr^{-1}.

From Apollo core samples, the median gardened depth z_g is, at a ~50% probability,

$$z_g(t) = 2.2t^{0.45} \tag{4}$$

where z_g is in units of cm and t is in Myr (Morris, 1978). This equation applies to timescales of ~0.1–1000 Myr (Costello et al., 2020). By combining Eq. (4) with Eq. (3), we find that

$$t_{SpWe}(t) = \frac{z_{SpWe}}{2.2} t^{0.55} \tag{5}$$

where t_{SpWe} is in units of Myr and z_{SpWe} is in cm (Fig. 2). This equation describes the median exposure time of the gardened soil.

Our assumption that all gardened soil has spent equal times at all depths is not quite correct, because the mixing time increases with depth (e.g., Costello et al., 2020). In other words, a deep grain would likely stay longer at its depth than would a shallower grain. This implies that Eq. (3) overestimates the amount of time that soil has spent at shallower depths. We note, however, that our approach estimates exposure timescales that are somewhat shorter than those found using the three-dimensional, lunar landscape evolution model developed by O'Brien and Byrne (2021). They found that, in a 3500 Myr old region, soil grains spend a median time of ~6 Myr in the top 0.1 cm. For the same age (3500 Myr) and depth ($z_{SpWe} = 0.1$ cm), Eq. (5) gives a median exposure time of 4 Myr, which is close to 6 Myr. The similarity between the results of their forward modeling and our more empirical approach gives us confidence that Eq. (5) provides an

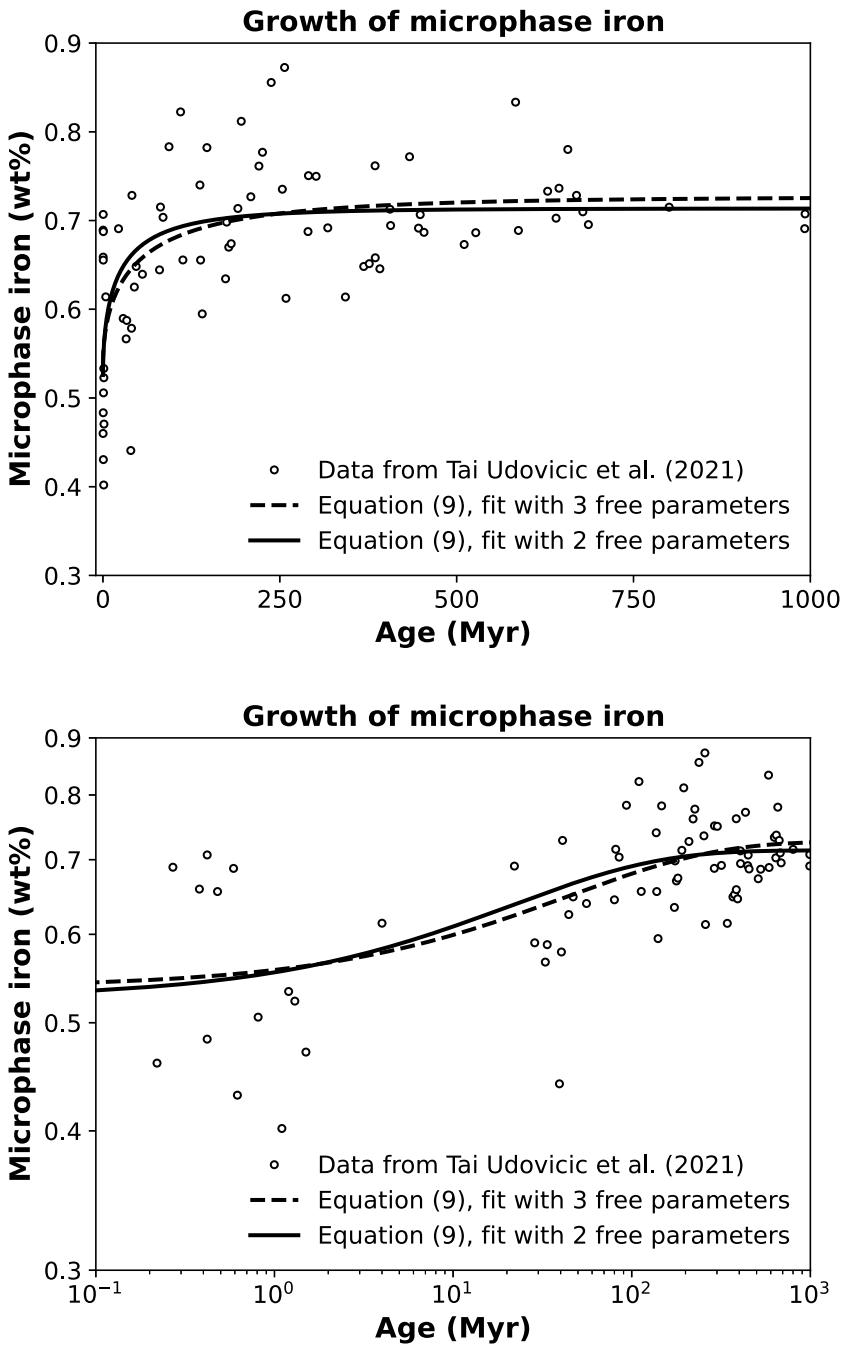

Fig. 4. How our model fits the abundance of microphase iron in the highlands as a function of soil age. Both plots show the same data and model output; the top has a linear scale and the bottom a logarithmic scale. The data are from the study of Tai Udovicic et al. (2021) (for uncertainties, please see their Fig. 3). The first best fit of Eq. (9) has three free parameters: $m_{max} = 0.73$ wt%, $m_{\Delta} = 0.19$ wt%, and $\sum_i (z_i/\tau_i) = 0.24$ cm Myr^{-1} (dashed curve). The other fit (solid curve) has two free parameters, since it uses $\sum_i (z_i/\tau_i) = 0.37$ cm Myr^{-1}, found from the npFe^0 data; here, $m_{max} = 0.71$ wt%, $m_{\Delta} = 0.19$ wt%.

adequate and straightforward way to calculate median exposure times to space weathering processes.

2.3. The model for the production of submicroscopic iron in the highlands

We combine Eqs. (2) and (5) to find how production of smFe^0 depends on time:

$$s(t) = s_{max} - s_{\Delta} \exp\left(-\frac{z_{SpWe}\, t^{0.55}}{2.2\ \tau_{SpWe}}\right) \tag{6}$$

If multiple space weathering processes are involved, z_{SpWe}/τ_{SpWe} should be replaced by $\sum_i (z_i/\tau_i)$, where z_i and τ_i are the characteristic depth and timescale of space weathering process i. The full equation is thus:

$$s(t) = s_{max} - s_{\Delta} \exp\left(-\frac{t^{0.55}}{2.2} \sum_i \frac{z_i}{\tau_i}\right) \tag{7}$$

3. Applying the model

We apply this model to the analysis of Tai Udovicic et al. (2021), who determined the abundance of smFe^0 in the ejecta of dated impact craters in the highlands. We fit Eq. (7) to their results for the abundances of mpFe^0 (>33 nm) and npFe^0 (<33 nm). This means our results are valid for the size-scales ($\gtrsim$10 km^2) of the ejecta annuli analyzed by

Tai Udovicic et al. (2021); they defined the inner edges of the annuli to be at the crater rims, i.e., at one crater radius, and the outer edges at four crater radii. We begin with $npFe^0$, because its growth rate is more constrained than that of $mpFe^0$.

Tai Udovicic et al. (2021) concluded that the initial ($t = 0$) abundance of $npFe^0$ in highland regolith is 0 wt%. Thus, we can use Eq. (7):

$$n(t) = n_{max}\left[1 - \exp\left(-\frac{t^{0.55}}{2.2}\sum_i \frac{z_i}{\tau_i}\right)\right] \quad (8)$$

where n is the abundance of $npFe^0$ (wt%), n_{max} is the steady-state abundance, and $n_\Delta = n_{max}$. We fit this equation to the $npFe^0$ data of Tai Udovicic et al. (2021) (Fig. 3) and find that the best fit is $n_{max} = 0.38$ wt% and $\sum_i(z_i/\tau_i) = 0.37$ cm Myr^{-1} ($R^2 = 0.9$, and the 1σ uncertainties in the fit parameters are 0.01 wt% and 0.03 cm Myr^{-1}). The timescale τ_{SpWe} is likely in the range of 1–10 Myr of exposure to the solar wind (Keller et al., 2021), and this should be the lower limit if other, more penetrative processes create $smFe^0$ (see Section 2.2). For this range of timescales, we find that the results of Tai Udovicic et al. (2021) constrain the functional depths of the combined space weathering processes to be $z_{SpWe} \gtrsim 0.3$–3 cm.

The situation for $mpFe^0$ is more complex because it contains two components. The first component is already present in the soil particles when they form, and the second is what is created subsequently by exposure to space weathering processes (Morris, 1980) (we discuss this in more detail in Section 4). Consequently, the initial abundance of $mpFe^0$ does not start at 0 wt% (Tai Udovicic et al., 2021). Thus, Eq. (7) becomes

$$m(t) = m_{max} - m_\Delta \exp\left(-\frac{t^{0.55}}{2.2}\sum_i \frac{z_i}{\tau_i}\right) \quad (9)$$

where m is the weight percent of $mpFe^0$, and m_Δ is the difference between the final abundance of $mpFe^0$ (m_{max}) and the initial abundance m_{min}. For the best fit, we find $m_{max} = 0.73$ wt%, $m_\Delta = 0.19$ wt%, and $\sum_i(z_i/\tau_i) = 0.24$ cm Myr^{-1} (the 1σ uncertainties in the fit parameters are, respectively, 0.02 wt%, 0.03 wt%, and 0.10 cm Myr^{-1}, and $R^2 = 0.4$) (solid curve in Fig. 4). Again, given the minimum 1–10 Myr found by Keller et al. (2021), the functional depth of the combined weathering processes is at least ~0.4–4 cm.

The significant scatter in the $mpFe^0$ data limits the conclusions we can draw from them, but we note that uncertainties in the values of $\sum_i(z_i/\tau_i)$ for both $npFe^0$ and $mpFe^0$ slightly overlap. In addition, if we use $\sum_i(z_i/\tau_i) = 0.37$ cm Myr^{-1} in Eq. (9), then the values for m_{max} and m_Δ change insignificantly, as does the goodness of the fit (dashed curve in Fig. 4). Thus, $\sum_i(z_i/\tau_i)$ is likely similar for both $mpFe^0$ and $npFe^0$, and we discuss the implications of this in the next section.

We can estimate the timescale needed to achieve a steady state in the abundance of both size ranges of $smFe^0$ on the size-scales analyzed by Tai Udovicic et al. (2021). According to our model, ~90% of the steady-state abundance of $npFe^0$ is created in ~100 Myr, ~95% in ~200 Myr, and ~99% in ~400 Myr. Because $mpFe^0$ does not start at 0 wt%, it reaches steady state more quickly: ~90% in ~30 Myr, ~95% in ~60 Myr, and ~99% in ~200 Myr. (We could do the same for total $smFe^0$ by adding Eqs. (8) and (9).) Consequently, we find that highland soils reach maturity in a few hundred million years, which agrees with analyses of Apollo samples (McKay et al., 1974) and agrees qualitatively with the analysis of Trang and Lucey (2019).

Our simple model successfully combines trends from a variety of data sets. Eq. (7) is based on a range of soil analyses – the maturity of Apollo cores as a function of depth, the surficial location of optically active $smFe^0$ in grains, the growth of grain rims and agglutinates – yet it describes orbital observations of space weathering. This correlative consistency gives us confidence that our model correctly describes how space weathering produces optically active $smFe^0$ in the lunar highlands.

4. Implications for space weathering in the lunar highlands

The success of our model places a significant constraint on the processes forming optically active $smFe^0$ in the highlands. Both $npFe^0$ and $mpFe^0$ are formed by processes with a depth-to-timescale ratio ($\sum_i(z_i/\tau_i)$) of about 0.3 cm Myr^{-1} (the average of the two ratios for the two size fractions). This suggests that both size fractions of $smFe^0$ could be formed by the same combination of processes.

We test this conclusion by finding the correlation between $smFe^0$ populations in the highlands. Beginning with $npFe^0$ and $mpFe^0$ abundance maps between ±60° latitude from Trang and Lucey (2019), we isolate the highlands using Nelson et al. (2014). We find the abundances of nanophase and microphase iron are well-correlated, with a Pearson coefficient of 0.60 (Fig. 5). Note that both $npFe^0$ and $mpFe^0$ have higher maximum values in Fig. 5 than in Figs. 3 and 4 because the values produced in the latter plots are averaged abundances over all pixels in an annuli surrounding the craters (Tai Udovicic et al., 2021). For this reason, we do not use those values to model the pixel-by-pixel relationship in Fig. 5.

Our analysis of orbital observations agrees with the analysis of Apollo soils done by Morris (1980). That author found that a soil's metallic iron has three components: (1) $npFe^0$, which is created by space weathering processes; (2) the fraction of $mpFe^0$ also created by those processes; and (3) the fraction of $mpFe^0$ native to the soil's source material. This last component is a constant for a given soil and depends on the amount of metallic iron in the rocks that have been comminuted to form the soil. This can be seen in Fig. 5: if $npFe^0$ is extrapolated to zero, i.e., extrapolated to unweathered soil, $mpFe^0$ would have a value of ~0.4 wt%. Furthermore, Morris (1980) showed that, as the soil matures, the abundances of $npFe^0$ and $mpFe^0$ are linearly correlated (the exact correlation depends on the soil's iron content, suggesting that our approach could be modified to apply to the maria). The agreement between Morris's analysis of lunar soils and our analysis of orbital observations gives us confidence that we have identified a linear correlation between $npFe^0$ and the maturity-dependent (i.e., time-varying) component of $mpFe^0$.

The correlation implies that <33 nm $smFe^0$ ($npFe^0$) is formed by the same processes, on the same timescales, and thus down to the same depths as the time-dependent (i.e., maturity-dependent) component of >33 nm $smFe^0$ ($mpFe^0$). The reason for this is that the equations for $n(t)$ and $m(t)$ (Eqs. (8) and (9)) both depend non-linearly on time. As a result, their depth-to-timescale ratios, i.e., $\sum_i(z_i/\tau_i)$, must be similar in order for the two quantities to be linearly correlated, reinforcing our conclusion in Section 3. It is unlikely that two different space weathering processes (e.g., the solar wind creating $npFe^0$ and micrometeoroid impacts creating $mpFe^0$) would have such similar (within 1σ) depth-to-timescale ratios. For this to occur, the relative difference in depths must be offset by the same relative difference in the timescales of formation. This seems to be unlikely, so we conclude that it is more reasonable that the linear correlation between $npFe^0$ and the time-dependent component of $mpFe^0$ implies that they are formed by the same set of processes.

Under the assumption that $npFe^0$ and $mpFe^0$ populations are formed by the same processes, and considering the critical ratio $\sum_i(z_i/\tau_i) \approx 0.3$ cm Myr^{-1}, we can make a determination about the processes most likely to form $smFe^0$. We rule out solar wind as an independent and significant contributor because the depth to which it processes the regolith is only the top layer of grains (i.e., solar wind ions cannot pass through grains)—too shallow to work over the modeled depths (~0.3–3 cm) and timescales (~1–10 Myr; see Fig. 1). Downward sputtered products (e.g., Hapke et al., 1975; Hapke, 2001) may penetrate to the next layer of grains but cannot pass through that layer, which is still not as deep as required by our model results.

On the other hand, the solar wind may still play an indirect role by aiding other, deeper processes in the formation of $smFe^0$. Solar wind-implanted hydrogen may help reduce iron during the impulsive heating

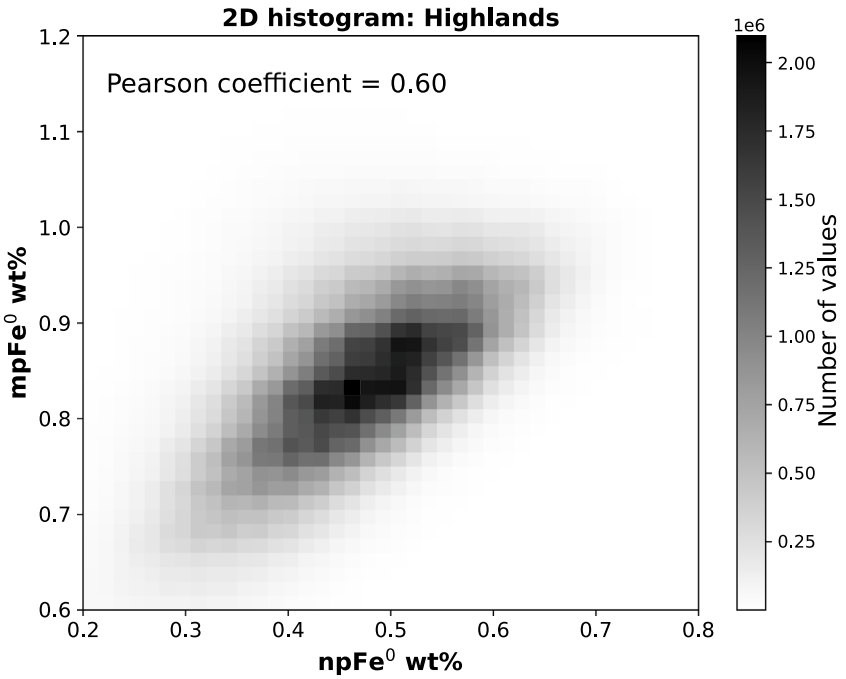

Fig. 5. A two-dimensional histogram of the abundances of npFe^0 and mpFe^0 in the highlands (~1 km/pixel at the equator). The two size fractions are well-correlated linearly, implying that they form on the same timescales and are thus created by the same space weathering process(es).

events – impacts and dielectric breakdown – that we discuss below (e.g., Housley et al., 1973; Allen et al., 1993). Although grains can be implanted with hydrogen only at the surface, impacts can distribute these grains throughout the gardened zone (e.g., see Section 2.2), where they are available to processes that operate deeper than the solar wind's penetration depth. Whether the solar wind does play such a role in the formation of smFe^0 is still uncertain, however, as some work has shown that vapor deposition can form smFe^0 without hydrogen implantation (Hapke et al., 1975; Hapke, 2001; Yamada et al., 1999; Sasaki et al., 2001, 2003).

Micrometeoroid impacts, on the other hand, may reasonably account for most optically active smFe^0, because they create both vapor deposits and agglutinates. The timescale on which they work is unclear, although it seems to be 1–10 Myr in terms of exposure to the solar wind (Keller et al., 2021). Since the solar wind is less penetrating than micrometeoroids, the exposure timescale to micrometeoroid weathering is likely longer. If so, then the characteristic penetration depth is $\gtrsim$0.1–1 cm.

This does not seem unreasonable for micrometeoroid impacts. We assume that micrometeoroids have masses $\lesssim 10^{-2}$ g (e.g., Hörz et al., 1991); in this case, the median mass of a micrometeoroid is $\sim 10^{-5}$ g (Grün et al., 1985). A projectile of this mass forms a crater with a depth of ~0.1 cm (Gault, 1973), assuming a speed of 10 km s^{-1} (Cintala, 1992), a micrometeoroid density of 3 g cm^{-3}, and a solid target of density 3 g cm^{-3} (McKay et al., 1991). (Note that ~0.1 cm represents the crater depth in a solid target, and so is a conservative estimate of the penetration depth in porous regolith. On the other hand, we assume a normally incident projectile, which overestimates the penetration depth, so we can assume that ~0.1 cm is reasonable for our purposes.) The median penetration depth of micrometeoroids is thus ~0.1 cm. A micrometeoroid of mass 10^{-2} g (the approximate upper limit for micrometeoroids) forms a crater with a depth of ~1 cm.

Consequently, about half of all micrometeoroid impacts affect depths ~0.1–1 cm and the rest affect depths $\lesssim$0.1 cm. This is in reasonable agreement with the characteristic penetration depth we estimated above ($\gtrsim$0.1–1 cm). Note that the time to garden to the approximate maximum depth of impacts, ~1 cm, is ~0.1 Myr. The youngest crater in Fig. 3 is 0.22 Myr, so $z_g \gtrsim z_{SpWe}$ for all the craters analyzed, and thus Eq. (5) can be used. As a result, it seems that micrometeoroid impacts can explain much of the abundance of optically active smFe^0.

Another possible source of smFe^0 is dielectric breakdown (herein referred to as "breakdown"), which has been predicted to occur in cold regions (e.g., much of the nightside) where large SEP events cause extreme deep dielectric charging (Jordan et al., 2014, 2019). If breakdown occurs, it likely creates vapor deposits (Jordan et al., 2015) and may create smFe^0 (Sheffer, 2007; Pasek et al., 2012). It is predicted to melt and vaporize soil at a rate comparable to that of micrometeoroid impacts (Jordan et al., 2019; Jordan, 2021) and thus may create smFe^0 on a similar timescale. In addition, it likely operates to depths of ~0.1 cm (Jordan et al., 2014), giving it a depth-to-exposure-time ratio of no more than ~0.01–0.1 cm Myr^{-1}. Thus, if breakdown weathering occurs, it may provide an additional source of smFe^0, consistent with the conclusions of Jordan (2021) and Jordan et al. (2022).

Other locations on the Moon may give the opportunity to further investigate these relations. In some permanently shadowed regions, the average solar wind flux is reduced by 2–3 orders of magnitude relative to the equator and at least an order of magnitude relative to their immediate surroundings (Rhodes and Farrell, 2020)—less than the estimated ~80% reduction at the swirl Reiner Gamma (Deca et al., 2018). Likewise, the micrometeoroid flux is somewhat reduced (Pokorný et al., 2020), but breakdown weathering is predicted to be enhanced, because these regions are cold throughout the lunar day (Jordan et al., 2015, 2017, 2019). Thus, permanently shadowed regions without exposed ice may further constrain the possible processes that dominate optical changes (e.g., Byron et al., 2019; Denevi and Robinson, 2020).

5. Conclusion

We created a simple model that describes the time-dependent accumulation of optically active smFe^0 in the lunar highlands. Our model synthesizes recent analyses of how space weathering processes form smFe^0-bearing agglutinates and rims on soil grains and how impact gardening controls the exposure time of the grains. It successfully reproduces the results of Tai Udovicic et al. (2021), particularly in regard

to npFe^0, showing that there is consistency among diverse analyses of Apollo samples and of orbital observations.

We find that our model results are not consistent with the solar wind directly forming smFe^0 (although the solar wind may play a role via hydrogen implantation). Our model results are consistent with highland smFe^0 being created mainly by micrometeoroid impacts, with a possible contribution from SEP-driven dielectric breakdown.

Acknowledgments

This work was supported by the NASA Solar System Exploration Research Virtual Institute, United States cooperative agreement number 80NSSC20M0021 (SSERVI's LEADER), and NASA, United States grants NNG11PA03C (LRO/CRaTER), NNG07EK00C (LRO/LROC), and 80NSSC21K1549 (FINESST). The solar wind rims data are from Keller et al. (2021), the submicroscopic iron data as a function of location on the Moon are publicly available via the Geosciences Node of the Planetary Data system: https://pds-geosciences.wustl.edu/missions/kaguya/trang_moon.htm, and the submicroscopic iron data are from Tai Udovicic et al. (2021). We thank David Trang and two anonymous reviewers for their help in improving this manuscript.

References

Allen, C.C., Morris, R.V., Lauer, H.V., J, McKay, D.S., 1993. Microscopic iron metal on glass and minerals—A tool for studying regolith maturity. Icarus 104, 291–300. http://dx.doi.org/10.1006/icar.1993.1102.

Arnold, J.R., 1975. Monte Carlo simulation of turnover processes in the lunar regolith. In: P. Lunar Planet. Sci. pp. 2375–2395.

Basu, A., 2005. Nanophase Fe0 in lunar soils. J. Earth Syst. Sci. 114, 375–380. http://dx.doi.org/10.1007/BF02702956.

Blewett, D.T., Denevi, B.W., Cahill, J.T.S., Klima, R.L., 2021. Near-UV and near-IR reflectance studies of lunar swirls: Implications for nanosize iron content and the nature of anomalous space weathering. Icarus 364, 114472. http://dx.doi.org/10.1016/j.icarus.2021.114472.

Britt, D.T., Pieters, C., 1994. Darkening in black and gas-rich ordinary chondrites: The spectral effects of opaque morphology and distribution. Geochim. Cosmochim. Acta 58, 3905–3919. http://dx.doi.org/10.1016/0016-7037(94)90370-0.

Byron, B.D., Retherford, K.D., Greathouse, T.K., Mand t, K.E., Hendrix, A.R., Poston, M.J., Liu, Y., Cahill, J.T., Mazarico, E., 2019. Effects of space weathering and porosity on the far-UV reflectance of amundsen crater. J. Geophys. Res. Planets 124, 823–836. http://dx.doi.org/10.1029/2018JE005908.

Cintala, M.J., 1992. Impact-induced thermal effects in the lunar and Mercurian regoliths. J. Geophys. Res. 97, 947–973. http://dx.doi.org/10.1029/91JE02207.

Costello, E.S., Ghent, R.R., Hirabayashi, M., Lucey, P.G., 2020. Impact gardening as a constraint on the age, source, and evolution of ice on mercury and the moon. J. Geophys. Res. Planets 125, e06172. http://dx.doi.org/10.1029/2019JE006172.

Deca, J., Divin, A., Lue, C., Ahmadi, T., Horányi, M., 2018. Reiner Gamma albedo features reproduced by modeling solar wind standoff. Commun. Phys. 1, 12. http://dx.doi.org/10.1038/s42005-018-0012-9.

Denevi, B.W., Robinson, M.S., 2020. Key science investigations of the moon's polar regolith — A nonvolatile perspective. In: Lunar Surface Science Workshop. p. 5122.

Domingue, D.L., Chapman, C.R., Killen, R., Zurbuchen, T.H., Gilbert, J.A., Sarantos, M., Benna, M., Slavin, J.A., Schriver, D., Trávníček, P.M., Orlando, T.M., Sprague, A.L., Blewett, D.T., Gillis-Davis, J.J., Feldman, W.C., Lawrence, D.J., Ho, G.C., Ebel, D.S., Nittler, L.R., Vilas, F., Pieters, C.M., Solomon, S.C., Johnson, C.L., Winslow, R.M., Helbert, J., Peplowski, P.N., Weider, S.Z., Mouawad, N., Izenberg, N.R., McClintock, W.E., 2014. Mercury's weather-beaten surface: Understanding mercury in the context of lunar and asteroidal space weathering studies. Space Sci. Rev. 181, 121–214. http://dx.doi.org/10.1007/s11214-014-0039-5.

Gault, D.E., 1973. Displaced mass, depth, diameter, and effects of oblique trajectories for impact craters formed in dense crystalline rocks. Moon 6, 32–44. http://dx.doi.org/10.1007/BF02630651.

Grün, E., Zook, H.A., Fechtig, H., Giese, R.H., 1985. Collisional balance of the meteoritic complex. Icarus 62, 244–272. http://dx.doi.org/10.1016/0019-1035(85)90121-6.

Hapke, B., 2001. Space weathering from Mercury to the asteroid belt. J. Geophys. Res. 106, 10,039–10,074. http://dx.doi.org/10.1029/2000JE001338.

Hapke, B., Cassidy, W., Wells, E., 1975. Effects of vapor-phase deposition processes on the optical, chemical, and magnetic properties of the lunar regolith. Moon 13, 339–353. http://dx.doi.org/10.1007/BF00567525.

Hemingway, D.J., Garrick-Bethell, I., Kreslavsky, M.A., 2015. Latitudinal variation in spectral properties of the lunar maria and implications for space weathering. Icarus 261, 66–79. http://dx.doi.org/10.1016/j.icarus.2015.08.004.

Hörz, F., Grieve, R., Heiken, G., Spudis, P., Binder, A., 1991. Lunar surface processes. In: Heiken, G.H., Vaniman, D.T., French, B. (Eds.), Lunar Sourcebook, A User's Guide to the Moon. pp. 61–120.

Housley, R., Grant, R.W., Paton, N.E., 1973. Origin and characteristics of excess fe metal in lunar glass welded aggregates. In: Lunar and Planetary Science Conference Proceedings, Vol. 4. p. 2737.

James, C.L., Letsinger, S.L., Basu, A., Wentworth, S.J., McKay, D.S., 2002. Size distribution of Fe0 globules in lunar agglutinitic glass. In: Lunar and Planetary Science Conference. p. 1827.

Jordan, A.P., 2021. Evidence for dielectric breakdown weathering on the Moon. Icarus 358, 114199. http://dx.doi.org/10.1016/j.icarus.2020.114199.

Jordan, A.P., Case, A.W., Wilson, J.K., Huang, C.-L., 2022. Evidence that earth's magnetotail affects dielectric breakdown weathering on the moon. Icarus 383, 115011. http://dx.doi.org/10.1016/j.icarus.2022.115011.

Jordan, A.P., Stubbs, T.J., Joyce, C.J., Schwadron, N.A., Spence, H.E., Wilson, J.K., 2013. The formation of molecular hydrogen from water ice in the lunar regolith by energetic charged particles. J. Geophys. Res. Planets 118, 1257–1264. http://dx.doi.org/10.1002/jgre.20095.

Jordan, A.P., Stubbs, T.J., Shusterman, M.L., Izenberg, N.R., Wilson, J.K., Hayne, P.O., Schwadron, N.A., Spence, H.E., 2019. How dielectric breakdown may contribute to the global weathering of regolith on the Moon. Icarus 319, 785–794. http://dx.doi.org/10.1016/j.icarus.2018.10.025.

Jordan, A.P., Stubbs, T.J., Wilson, J.K., Schwadron, N.A., Spence, H.E., 2015. Dielectric breakdown weathering of the moon's polar regolith. J. Geophys. Res. Planets 120, 210–225. http://dx.doi.org/10.1002/2014JE004710.

Jordan, A.P., Stubbs, T.J., Wilson, J.K., Schwadron, N.A., Spence, H.E., 2017. The rate of dielectric breakdown weathering of lunar regolith in permanently shadowed regions. Icarus 283, 352–358. http://dx.doi.org/10.1016/j.icarus.2016.08.027.

Jordan, A.P., Stubbs, T.J., Wilson, J.K., Schwadron, N.A., Spence, H.E., Joyce, C.J., 2014. Deep dielectric charging of regolith within the moon's permanently shadowed regions. J. Geophys. Res. Planets 119, 1806–1821. http://dx.doi.org/10.1002/2014JE004648.

Keller, L.P., Berger, E.L., Zhang, S., Christoffersen, R., 2021. Solar energetic particle tracks in lunar samples: A transmission electron microscope calibration and implications for lunar space weathering. Meteorit. Planet. Sci. 168, 5–1707. http://dx.doi.org/10.1111/maps.13732.

Keller, L.P., Clemett, S.J., 2001. Formation of nanophase iron in the lunar regolith. In: 32nd Lunar and Planetary Science Conference. p. 2097.

Keller, L.P., McKay, D.S., 1997. The nature and origin of rims on lunar soil grains. Geochim. Cosmochim. Acta 61, 2331–2341. http://dx.doi.org/10.1016/S0016-7037(97)00085-9.

Keller, L.P., Wentworth, S.J., McKay, D.S., Taylor, L.A., Pieters, C., Morris, R.V., 2000. Space weathering in the fine size fractions of lunar soils: Mare/highland differences. In: 31st Lunar and Planetary Science Conference. p. 1655.

Kramer, G.Y., Combe, J.P., Harnett, E., Hawke, B.R., Noble, S.K., Blewett, D.T., McCord, T.B., Giguere, T.A., 2011. Characterization of lunar swirls at mare ingenii: A model for space weathering at magnetic anomalies. J. Geophys. Res. Planets 116 (E04008), http://dx.doi.org/10.1029/2010JE003669.

Lucey, P.G., 2006. Radiative transfer modeling of the effect of mineralogy on some empirical methods for estimating iron concentration from multispectral imaging of the moon. J. Geophys. Res. Planets 111 (E08003), http://dx.doi.org/10.1029/2005JE002661.

Lucey, P.G., Riner, M.A., 2011. The optical effects of small iron particles that darken but do not redden: Evidence of intense space weathering on Mercury. Icarus 212, 451–462. http://dx.doi.org/10.1016/j.icarus.2011.01.022.

McFadden, J., Garrick-Bethell, I., Sim, C.K., Kim, S.S., Hemingway, D., 2019. Iron content determines how space weathering flux variations affect lunar soils. Icarus 333, 323–342. http://dx.doi.org/10.1016/j.icarus.2019.05.033.

McKay, D.S., Fruland, R., Heiken, G.H., 1974. Grain size and the evolution of lunar soils. In: Lunar and Planetary Science Conference Proceedings. pp. 887–906.

McKay, D.S., Heiken, G., Basu, A., Blanford, G., Simon, S., Reedy, R., French, B., Papike, J., 1991. The lunar regolith. In: Heiken, G., Vaniman, D., French, B.M. (Eds.), Lunar Sourcebook. Cambridge Univ., Cambridge, pp. 285–356.

Mendell, W.W., McKay, D.S., 1975. A lunar soil evolution model. Moon 13, 285–292. http://dx.doi.org/10.1007/BF00567520.

Morris, R.V., 1978. In situ reworking (gardening) of the lunar surface - Evidence from the Apollo cores. In: P. Lunar Planet. Sci. pp. 1801–1811.

Morris, R.V., 1980. Origins and size distribution of metallic iron particles in the lunar regolith. In: Lunar and Planetary Science Conference Proceedings 2. pp. 1697–1712.

Nelson, D.M., Koeber, S.D., Daud, K., Robinson, M.S., Watters, T.R., Banks, M.E., Williams, N.R., 2014. Mapping lunar maria extents and lobate scarps using lroc image products. In: 45th Annual Lunar and Planetary Science Conference. In: Lunar and Planetary Science Conference, p. 2861.

Noble, S.K., Pieters, C., Keller, L.P., 2007. An experimental approach to understanding the optical effects of space weathering. Icarus 192, 629–642. http://dx.doi.org/10.1016/j.icarus.2007.07.021.

O'Brien, P., Byrne, S., 2021. Physical and chemical evolution of lunar mare regolith. J. Geophys. Res. Planets 126, e06634. http://dx.doi.org/10.1029/2020JE006634.

Pasek, M.A., Block, K., Pasek, V., 2012. Fulgurite morphology: a classification scheme and clues to formation. Contrib. Miner. Pet. 164, 477–492. http://dx.doi.org/10.1007/s00410-012-0753-5.

Pieters, C., Fischer, E.M., Rode, O., Basu, A., 1993. Optical effects of space weathering: The role of the finest fraction. J. Geophys. Res. 98, 20817–20824. http://dx.doi.org/10.1029/93JE02467.

Pieters, C.M., Noble, S.K., 2016. Space weathering on airless bodies. J. Geophys. Res. Planets 121, 1865–1884. http://dx.doi.org/10.1002/2016JE005128.2016JE005128.

Pokorný, P., Sarantos, M., Janches, D., Mazarico, E., 2020. Meteoroid bombardment of lunar poles. Astrophys. J. 894, 114. http://dx.doi.org/10.3847/1538-4357/ab83ee, arXiv:2003.12640.

Rhodes, D.J., Farrell, W., 2020. Mapping the predicted solar wind hydrogen flux in lunar south pole craters. Planet. Sci. J. 1, 13. http://dx.doi.org/10.3847/PSJ/ab8939.

Sasaki, S., Kurahashi, E., Yamanaka, C., Nakamura, K., 2003. Laboratory simulation of space weathering: Changes of optical properties and TEM/ESR confirmation of nanophase metallic iron. Adv. Space Res. 31, 2537–2542. http://dx.doi.org/10.1016/S0273-1177(03)00575-1.

Sasaki, S., Nakamura, K., Hamabe, Y., Kurahashi, E., Hiroi, T., 2001. Production of iron nanoparticles by laser irradiation in a simulation of lunar-like space weathering. Nature 410, 555–557.

Sheffer, A.A., 2007. Chemical Reduction of Silicates by Meteorite Impacts and Lightning Strikes (Ph.D. thesis). University of Arizona.

Sim, C.K., Kim, S.S., Lucey, P.G., Garrick-Bethell, I., Choi, Y.J., 2017. Asymmetric space weathering on lunar crater walls. Geophys. Res. Lett. 44, 11,273–11,281. http://dx.doi.org/10.1002/2017GL075338.

Tai Udovicic, C.J., Costello, E.S., Ghent, R.R., Edwards, C.S., 2021. New constraints on the lunar optical space weathering rate. Geophys. Res. Lett. 48, e2020GL092198. http://dx.doi.org/10.1029/2020GL092198.

Taylor, L.A., Pieters, C., Keller, L.P., Morris, R.V., McKay, D.S., 2001. Lunar mare soils: Space weathering and the major effects of surface-correlated nanophase Fe. J. Geophys. Res. 106, 27985–28000. http://dx.doi.org/10.1029/2000JE001402.

Taylor, L.A., Pieters, C., Patchen, A., Taylor, D.H.S., Morris, R.V., Keller, L.P., McKay, D.S., 2010. Mineralogical and chemical characterization of lunar highland soils: Insights into the space weathering of soils on airless bodies. J. Geophys. Res. Planets 115 (E02002), http://dx.doi.org/10.1029/2009JE003427.

Trang, D., Lucey, P.G., 2019. Improved space weathering maps of the lunar surface through radiative transfer modeling of Kaguya multiband imager data. Icarus 321, 307–323. http://dx.doi.org/10.1016/j.icarus.2018.11.014.

Yamada, M., Sasaki, S., Nagahara, H., Fujiwara, A., Hasegawa, S., Yano, H., Hiroi, T., Ohashi, H., Otake, H., 1999. Simulation of space weathering of planet-forming materials: Nanosecond pulse laser irradiation and proton implantation on olivine and pyroxene samples. Earth Planets Space 51, 1265. http://dx.doi.org/10.1186/BF03351599.